Observations of colocated optical and radar aurora

H. Bahcivan,[1] D. L. Hysell,[2] D. Lummerzheim,[3] M. F. Larsen,[4] and R. F. Pfaff[5]

[1] This article presents case studies of common volume observations of the E region radar aurora obtained with a 30 MHz imaging radar and the optical aurora (green line emissions) recorded by an all sky camera. In addition, in situ rocket electric field measurements in the vicinity of an auroral arc are presented in a separate case study. As inferred from the measurements, the radar aurora in the vicinity of a stable evening auroral arc arises because of the arc's polarization electric fields, which excite the two stream instability and generate electron density irregularities at meter scales. The radar aurora is the backscattering of radar waves from these irregularities.

1. Background

[2] In March of 2003, a 30 MHz imaging radar in Anchorage was operated jointly with an all sky camera in Poker Flat, Alaska as part of the NASA JOULE sounding rocket campaign, which was carried out to determine the contribution to Joule heating from the fluctuating features of auroral convection. The experiments also provided an opportunity to compare radar and optical measurements in order to investigate the role of auroral arcs in the generation of meter-scale plasma density irregularities giving rise to radar backscatter.

[3] Plasma instabilities driven by electric fields and/or plasma density gradients are responsible for meter-scale irregularities. The two instabilities that are predicted to best function in the auroral E region are the two stream instability and the gradient drift instability. *Fejer et al.* [1975] presents the dispersion relation governing the irregularities, and the expressions for the wave frequency and the growth rate. In the absence of ion drifts and for magnetized electrons, the two stream wave growth requires an electric field above a threshold, while the gradient drift wave growth requires a sufficient density gradient and an electric field with the right sign. Both electric fields and density gradients are present in the vicinity of auroral arcs. Therefore both instabilities may occur. In the conclusion of this paper, we will argue that the electric field is the key parameter for radar aurora.

[4] There have been coherent and incoherent scatter radar soundings of the E region in conjunction with all sky camera observations. *Balsley et al.* [1973] and *Greenwald et al.* [1973] carried out studies with a narrow beam VHF radar located in Anchorage, Alaska and reported a close correspondence between visual auroral and VHF radar auroral forms. In particular, *Greenwald et al.* [1973] made a distinction between "diffuse radar aurora" and "discrete radar aurora" based on their appearance on a range-time-intensity plot. Comparison of all sky camera images with the radar data indicated that the diffuse (discrete) radar aurora occurs in a latitudinal zone on the equatorward (poleward) side of the visual auroral activity. *Tsunoda et al.* [1976] constructed radar echo maps with a 398-MHz phased array radar located at Homer, Alaska. They similarly found that discrete visual arcs occur poleward of the diffuse radar aurora. The discrete radar echoes were mostly associated with only bright visual arcs. *Providakes et al.* [1985] carried out VHF radar interferometer observations of E region plasma irregularities associated with discrete auroral arcs and reported strong arc-associated polarization electric field, narrow radar backscattering structures aligned parallel to the poleward edges of the arcs, and diffuse backscatter from the equatorward edges. *Prikryl and Cogger* [1992] found that stronger VHF radar returns predominantly occur on the remote (poleward) side of the optical aurora, where the aspect angle conditions were optimal. In the premidnight sector, some of the brightest aurora were found to be coincident with the strongest radar returns, and a significant fraction of weaker radar echoes occurred equatorward of fainter auroral forms. Recently, *Milan et al.* [2001] presented E region HF radar backscatter measurements along with simultaneous observations of auroral luminosity from all-sky cameras. The L-shell aligned backscatter occurred in a region of low luminosity bounded to the north and south by two auroral arcs. Moreover, *Milan et al.* [2003] detected particularly sharp backscattering boundaries at the edges of auroral arcs and described variations in the echo characteristics in association with the arc's electrodynamical structure.

[5] It is possible that some of the previous findings from HF radars suffered from limited precision in locating the

[1]Center for Geospace Studies, SRI International, Menlo Park, California, USA.
[2]Earth and Atmospheric Sciences, Cornell University, Ithaca, New York, USA.
[3]Geophysical Institute, University of Alaska, Fairbanks, Alaska, USA.
[4]Department of Physics and Astronomy, Clemson University, Clemson, South Carolina, USA.
[5]NASA Goddard Space Flight Center, Greenbelt, Maryland, USA.

source of the backscatter. HF radars are more subject to refraction than VHF radars, which implies altitude and range ambiguity. Moreover, because auroral echoes are less aspect sensitive at HF frequencies [*Watermann*, 1990] and exhibit considerable dynamic range, there is added uncertainty as to the location of the scattering volume.

[6] A 30 MHz imaging coherent scatter radar can contribute by providing relatively unambiguous power and Doppler velocity measurements in the *E* region with high temporal and spatial resolution. Refraction of the 30 MHz signal introduces less uncertainty in the backscatter altitude. Ambiguity in azimuth and elevation of the backscatter is resolved using interferometry and aperture synthesis imaging [*Hysell and Chau*, 2006]. Moreover, spectra can be computed using standard pulse-to-pulse radar techniques and do not suffer from clutter and spectral resolution problems associated with double pulses and multipulses. An application of radar imaging with this radar was successfully demonstrated by *Bahcivan et al.* [2005] where common volume radar and rocket observations of *E* region irregularities were used to describe radar spectral characteristics as a function of the vector electric field.

[7] We next describe the radar aurora associated with a system of intense evening arcs. Then, we describe a sequence of events inferred from rocket measurements made during a separate auroral arc event.

2. Data Presentation

[8] The data used in this study are from three sets of instruments operated in support of the NASA JOULE sounding rocket campaign from Poker Flat Research Range in Alaska in March 2003. Poker Flat is located at the magnetic latitude of 65.60 N.

[9] The white-light (unfiltered) optical measurements were made by the Poker Flat all sky camera operated by the University of Alaska at Fairbanks, Alaska. To characterize the emissions and to infer the main altitude of the white light, we refer to the Poker Flat meridian scanning photometer data.

[10] The radar used for this investigation is the Clemson/Cornell 30 MHz coherent scatter radar imager located at the High Latitude Monitoring Station (HLMS) run by the University of Alaska Fairbanks on Elmendorf Air Force Base in Anchorage, Alaska. This is a single-beam pulsed Doppler radar that uses interferometry with five receiving antennas and multiple interferometry baselines to recon-
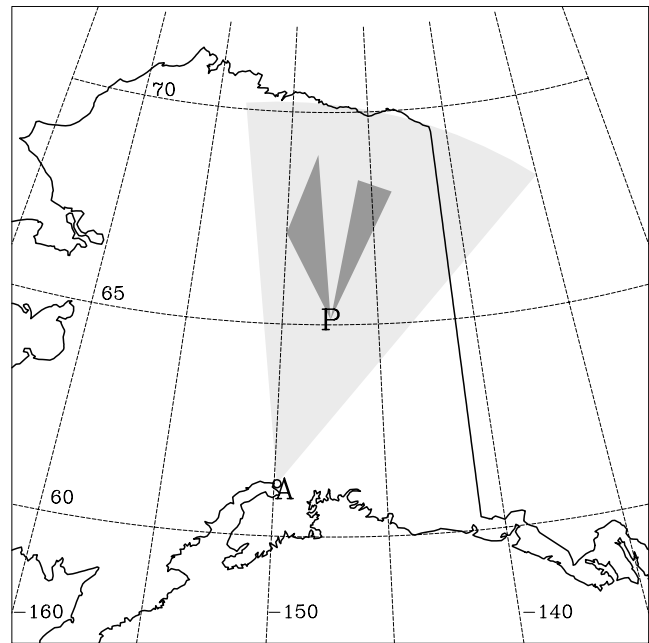
Figure 1. Diagram of the JOULE experiment showing locations of the 30 MHz radar at Anchorage (A) and the Poker Flat Rocket Range (P). The light gray sector represents the angular coverage of the radar. The dark sectors are the rocket launch corridors. Instrumented and chemical release rockets were launched along each of these corridors.

struct images of the backscatter in three-dimensional range and bearing space. Details about radar imaging in general and the inversion algorithm applied here in particular can be found in the work of *Hysell* [1996] and most recently in the work of *Hysell and Chau* [2006]. Table 1 lists the parameters of the radar. The interpulse period (IPP) for the experiments was 2.83 ms, corresponding to 425 km, and the echoes observed are presumed to have ranges between 425 and 850 km.

[11] The light gray sector in Figure 1 represents the angular coverage of the radar from a large perspective. The actual imaged region spans the area across the bore sight, as marked by the yellow boundaries in Figure 4. However, the radar waves intercept the *E* region altitudes over some of this region with near perpendicularity. In order to address the aspect angle of the echoes, we have carried out ray tracing calculations, assuming a horizontally stratified *E* region ionosphere with an electron density profile based on the profiles measured by the instrumented rocket payloads (to be described next) during the JOULE campaign. The results are shown in Figure 2. The left panel represents the altitude where the condition for field-aligned backscatter is exactly met for a 30 MHz radar in Anchorage, and the right panel shows the aspect angle at an altitude of 115 km for the same conditions. Elevation angle information arising as a byproduct of radar imaging reveals that most of our echoes arrive from altitudes between 110 and 120 km. Both figures illustrate that the nominal scattering geometry differs greatly across the imaged area.

[12] The third set of instruments includes the electric field and density measurement apparatus on board two of the

Table 1. The 30 MHz Radar Parameters

Parameter	Value	Units
Frequency	29.8	MHz
Peak power	8	kW
Duty cycle	7.6	percent
HPFB	10	deg
IPP	425	km
Pulse length	32.5	km
Pulse code (Barker)	13 bit	
Bandwidth	10	μs
Range resolution	2.5	km
Time resolution	5	s
Azimuth resolution	0.4	deg.
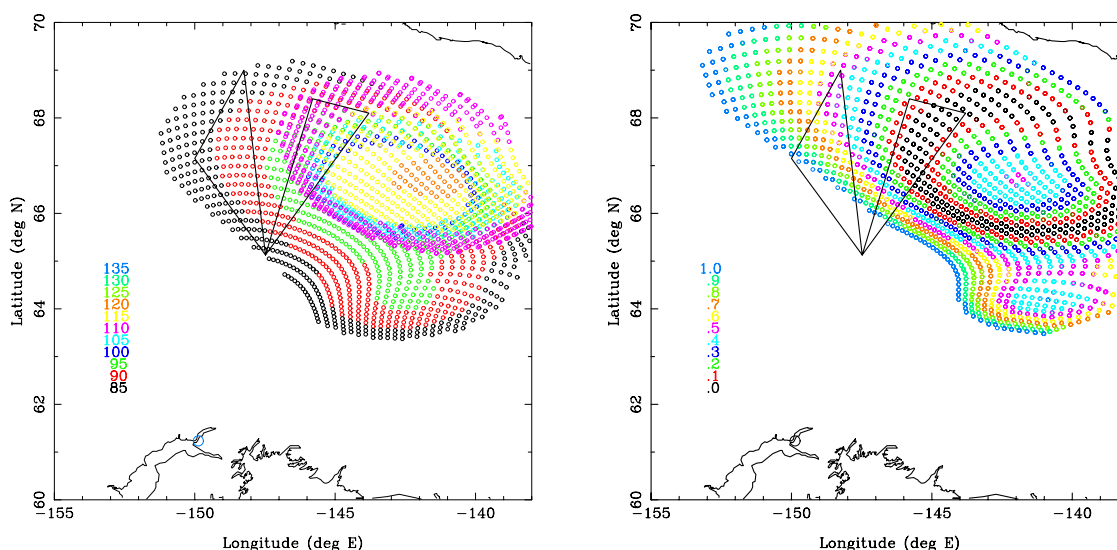
Figure 2. Raytracing calculations of the Bragg scattering condition for field-aligned backscatter for a 30 MHz radar in Anchorage. Density profiles measured (on 27 March 2003) during the JOULE campaign were incorporated into the calculations. (left) Altitude where perpendicularity occurs. (right) Aspect angle at a fixed altitude of 115 km.

sounding rockets, which were launched toward geographic north and north-northeast on 27 March 2003 at 0309 LT (1209 UT) and 0312 LT (1212 UT) from the Poker Flat Research Range near Fairbanks, Alaska. The trajectories for the two rockets were along the two corridors shown in Figure 1. The rocket measurements will be presented in a separate case study toward the end of this paper.

2.1. Radar and Optics Data From 1 March 2003

[13] For radar and optics comparison, we first focus on the data taken between 0900 and 1015 UT (UT = LT + 9) on 1 March (Day 60), 2003, coinciding with a set of electrojet intensifications over Poker Flat. The auroral convection deduced by the SuperDARN radar network [*Greenwald*, 1995] based on *F* region backscatter measurements from a set of radar locations showed that the observations were made at a time preceding the high-latitude convection reversal. Significant *F* region radar backscatter was recorded at 0900 UT, the Doppler velocities, indicating that the convection pattern over Poker Flat was mainly south-westward. The convection at this time was consistent with the Doppler shifts observed by the 30 MHz radar [*Bahcivan*, 2005]. After approximately 910 UT until the end of the observation period, however, it is difficult to describe a particular pattern for the 30 MHz radar Doppler shifts and SuperDARN network did not record significant echoes over the imaged region.

[14] The Poker Flat magnetometer (http://www.gedds.alaska.edu/) showed its first major deflections (100–150 nT) at 0900 UT as seen in the top panel of Figure 3. The first negative deflections of the H and D components at 0900 UT imply northward and westward intensification of the auroral electrojet. Similar deflections occurred around 0940 and 1005 UT.

[15] The first major magnetic deflections also mark the beginning of auroral activity as observed by the ultraviolet imager on board NASA's Polar spacecraft. The activity was first confined to a small region around 60 MLat near magnetic midnight (0858 UT) and rapidly spread over Alaska longitudes in the west within minutes, which can be identified from the Poker Flat all sky camera observations as the brightening of a system of east-west aligned arcs that occurred between 0900 and 0905 UT around 62 MLat. This was followed by an equatorward expansion of aurora to 58 MLat and rapid poleward expansion to 69 MLat. By 0915 UT, the expansion was followed by a stable, geomagnetic east-west oriented arc between 65 and 68 MLat, below which there was no noticeable emissions left. The new arc gradually moved equatorward and began to expand into a system of arcs at 0930 UT. At 0940 UT, a rapid and narrow auroral intensification occurred between 67 and 68 MLat with the same geomagnetic east-west alignment. Between 1000 and 1010 UT, several bands of northwest-southeast aligned arc formations propagated westward.

[16] The summary time series data of radar and optical aurora in the form of range-time-intensity plots are shown in the middle and bottom panels of Figure 3, respectively. The original optical data time series were given as a function of geomagnetic north-south elevation and time, and the radar bore sight is approximately in the geomagnetic north direction. We mapped the elevation on the radar bore sight range line.

[17] Both radar and optical activity began with relatively faint equatorward drifting forms prior to 0900 UT. Then, the radar data showed bursts of activity between 0900 and 0905 UT, between 0940 and 0945 UT, and between 1000 and 1010 UT, coinciding with the times of arc intensifications. After approximately 1015 the radar activity ceased, although the optical activity persisted in the form of diffuse auroral emissions. Comparing the radar and all sky camera observations from Figure 3, the radar aurora appears to be more closely associated with discrete rather than diffuse auroral forms.

[18] Figure 4 shows samples of radar aurora images (in color) superimposed on white optical images (in gray scale).
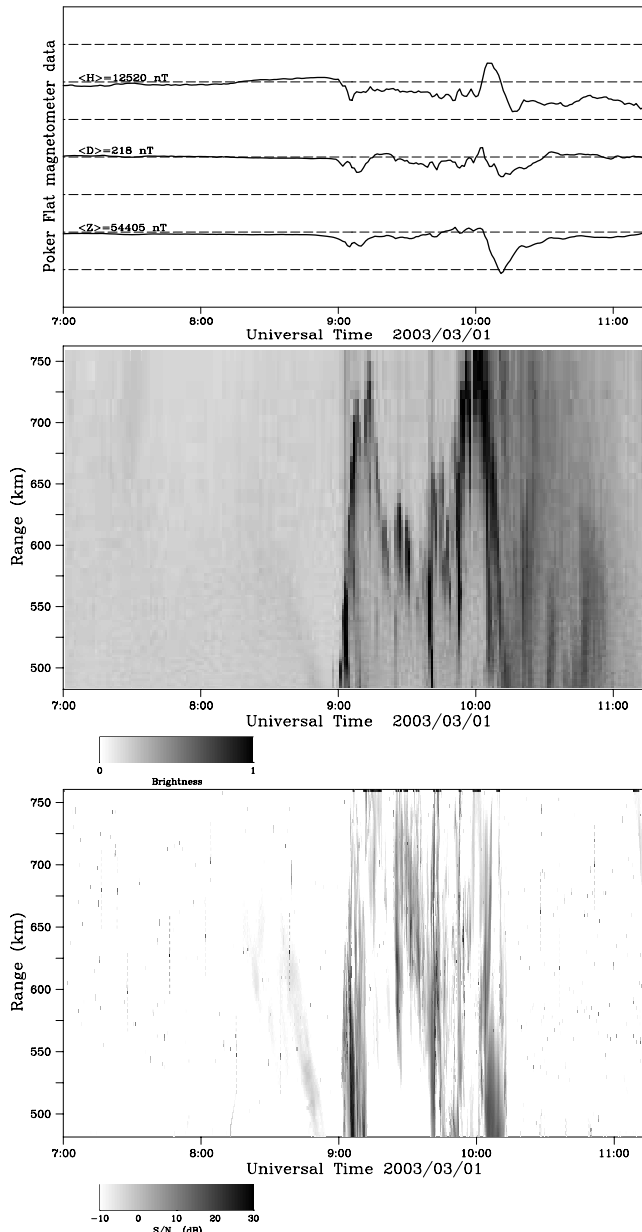
Figure 3. (top) Time series of Poker Flat magnetometer deviations. The vertical grid is 250 nano-Tesla/grid line. The mean values for the day are shown on the left-hand side, in nT units. Positive deflections of H, D, and Z components indicate geomagnetic northward, eastward, and vertical magnetic field deflections, respectively. (Data source: Geophysical Institute, University of Alaska, Fairbanks). (middle) Summary of all sky camera data. (bottom) Radar range-time intensity. The range is the radar line-of-sight distance to the E region from the 30 MHz radar in Anchorage, Alaska.

The radar images are computed by applying radar interferometry to 5 s incoherent integrations of radar backscatter data. The yellow line marks the imaged radar backscatter region boundary. The radar image pixels span 2.5 km in range and, depending on the range, $3-5$ km in azimuth. The brightness of each radar image pixel represents the signal-to-noise ratio on a logarithmic scale. The hue represents the Doppler shift spanning between ± 888 m/s, with blue and red shifts representing echoes coming toward and going away from the radar, respectively. That sharp Doppler shift gradients are real and will be used to infer the presence of flow shears and field-aligned currents associated with the arcs. Note that because of the field-aligned irregularity condition for radar backscatter, certain areas in the radar image are more likely to give rise to echoes (see Figure 2 for the optimally scattering regions).

[19] The optical images in Figure 4 are unwrapped for 100 km altitude and the optical content represents a 1/30 s exposure. The times are chosen so that the radar images are constructed when the optical aurora is almost overhead so that the localization of optical emissions does not suffer from distortions during unwrapping. To characterize the emissions and to infer the main altitude of the white light, we referred to the Poker Flat meridian scanning photometer data. The summary data for the green line emissions (557.6 nm) and N_2^+ emissions (427.8 nm) very closely followed the space and time structuring in the all sky camera summary data shown in the top panel of Figure 3. On the other hand, the red line emissions (630.0 nm) were evenly spread from horizon to horizon, having almost uniform intensity for the observation period. This lets us conclude that the brightness in the optical images mostly represents green line and N_2^+ emissions, which mainly originate in the E region.

[20] The cases shown in Figure 4 are representative of an animated sequence spanning the observation period of an hour and a quarter. A summary of relative radar optics localization based on this sequence is as follows. As we infer from the backscatter intensity and Doppler velocities, the localization and evolution of radar aurora and optical aurora are very much connected. First, a stable auroral arc is often accompanied by a stable radar aurora located at the arc's edges. If the arc's alignment is slowly distorted the radar aurora closely follows the distortion. As the distortion is increased and nearby arcs are generated, the localization of radar aurora is often unpredictable. At the peak of an intensification, radar aurora can be seen within the very bright regions in some cases. Following an intensification and when equatorward and poleward expansion occurs, the radar aurora contains localized, rapidly evolving structures located anywhere in between the poleward and equatorward boundaries of the disturbed region. The poleward edges of the east-west aligned and elongated arcs located at the poleward side of the disturbed region are mostly accompanied by narrow radar backscattering structures aligned parallel to the arcs. The backscattering regions from the equatorward edges of east-west aligned equatorward arcs are wider. Although there were other periods potentially suitable for radar imaging and optical analysis, the processing of the radar images requires a substantial effort and a statistical study of joint radar optical aurora occurrence as a function of magnetic local time will be considered for future studies.

2.2. Radar, Optics, and Rocket Data From 27 March 2003

[21] In this section, we present a comparison of the rocket, radar, and optics measurements in the neighborhood of an arc. There were two instrumented rockets launched as
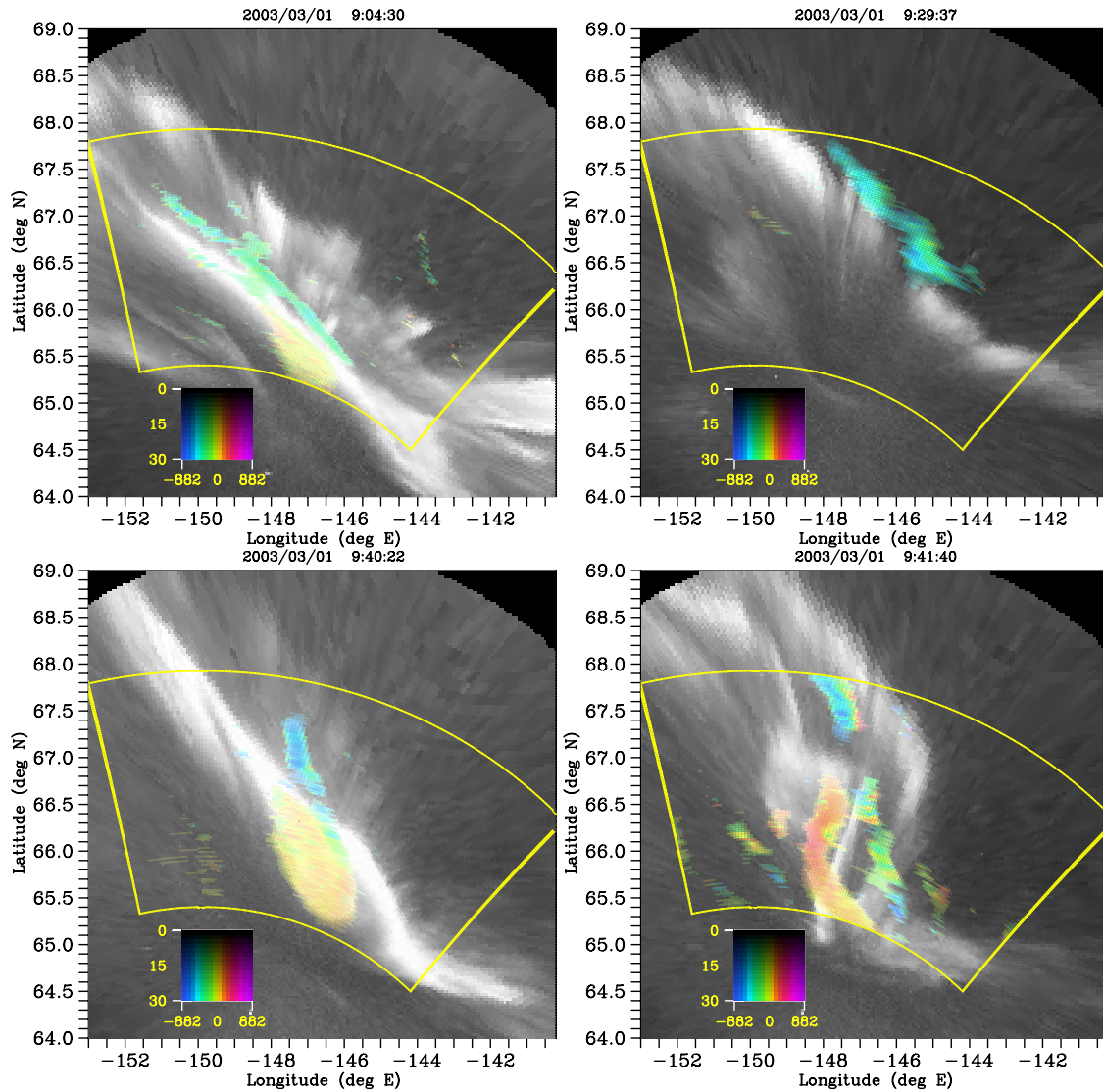
Figure 4. Poker Flat all sky camera image (gray scale) unwrapped to geodetic coordinates for 100 km altitude with the corresponding radar images (in color) superimposed.

part of the JOULE campaign. The rockets were launched with 3 min separation, the first one at 1209 UT and the second one at 1212 UT, on 27 March 2003 from the Poker Flat Research Range near Fairbanks, Alaska. They were launched toward geographic north and north northeast. The trajectories for the two rockets were along the two corridors shown in Figure 1.

[22] The day of 27 March was geomagnetically very active, with magnetometer deflections reaching 500 nT (see Figure 5) but during the rocket launches the magnetometer activity was moderate (200–250 nT). During the rocket flights (1209–1218 UT) the Poker Flat magnetometer appears to be recovering from major deflections that occurred around 1200 UT. SuperDARN convection plots suggest that the convection was in transition from southward to eastward. The optical data show no intensifications around Poker Flat, but later toward the end of the rocket flights some activity picks up in the north.

[23] Our emphasis will be the deflections of in situ electric field recordings in approach to an auroral arc and
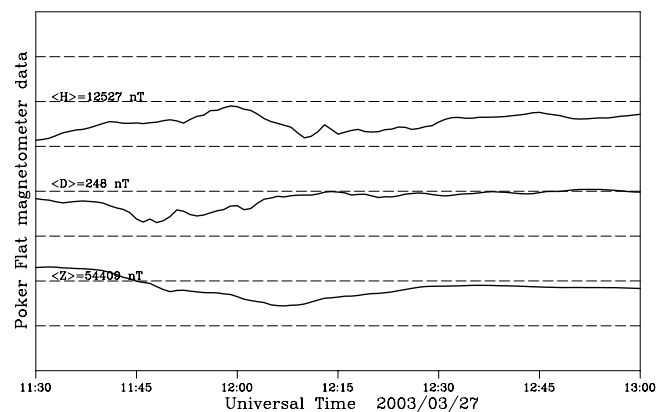

Figure 5. Time series of Poker Flat magnetometer deviations for 27 March 2003 (see magnetometer data description in Figure 3).
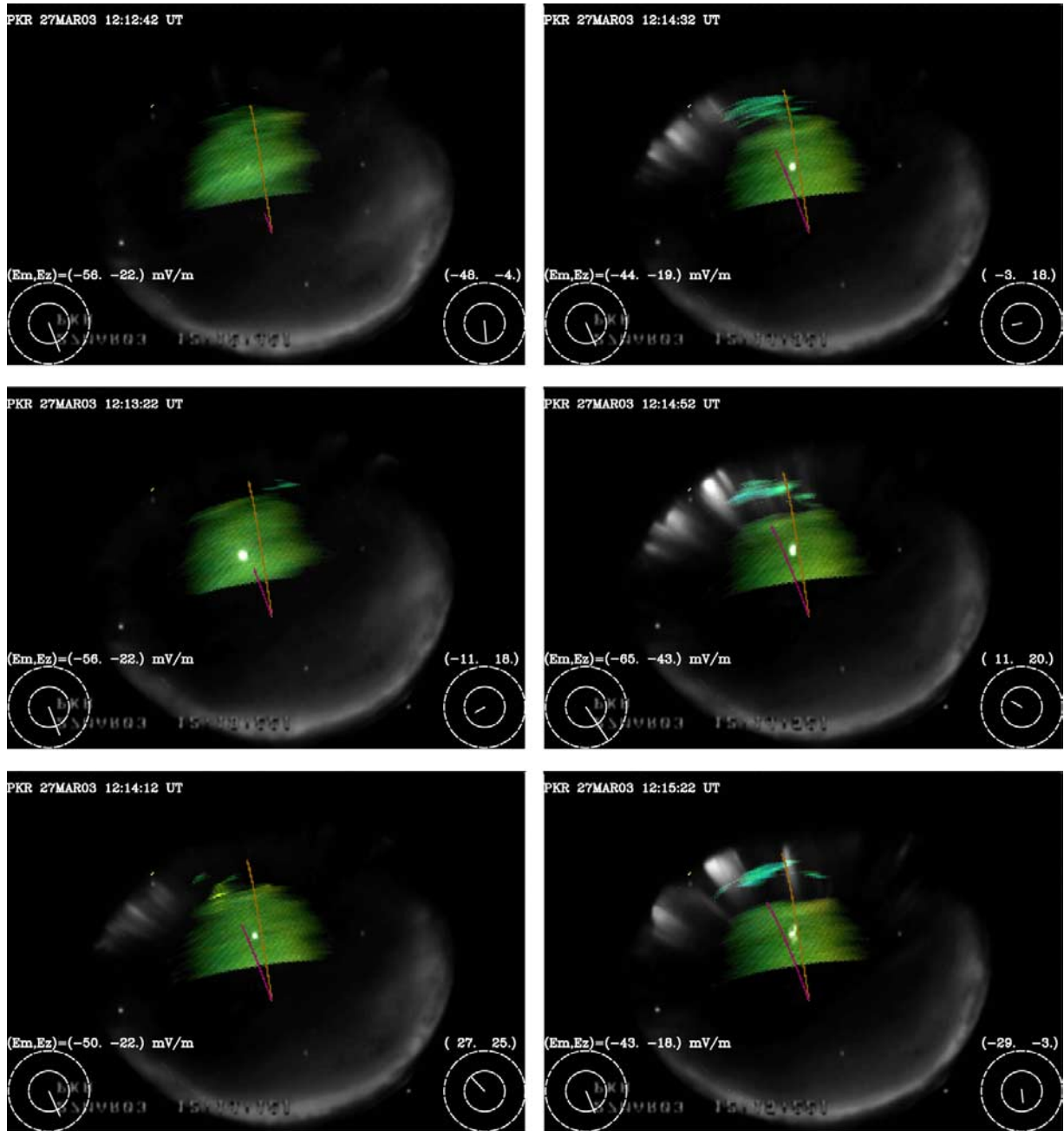
Figure 6. A set of images displaying superimposed optics, radar and rocket data. The times are 1242, 1322, 1412, 1432, 1452, and 1522 minutes past 1200 UT with images ordered as in a double-column text. See text for further explanations.

radar backscatter observations. Figure 6 shows data from several instants of joint optical, radar, and in situ rocket measurements. The snapshots are ordered as in a "double-column" text. The radar images represent the same 5 s integration, but the optical content here represents a 30 s integration. This long optical integration period was chosen because the auroral brightness was dim, perhaps because the auroral arc was just appearing in the northern horizon. Superimposed on the radar and optical images are the rocket trajectories mapped along the magnetic field lines to the E region. Note that a vertical cut through the round all sky camera view is aligned in the magnetic north-south direc-tion, the bottom of the circular area being the southern horizon. The dial monitor on the left (right) corresponds to the red (yellow) rocket trajectory. The vectors on the dial monitors indicate the electric field magnitude and direction relative to the background image. The values above the dial monitors are the electric field components in mV/m: mag-netic north (first number) and magnetic west (second number). The electric fields are mapped along the geomag-netic field lines to the E region altitudes. We avoided plotting the images in geographic or geomagnetic coordi-nates because the aurora is at the horizon and unwrapping of auroral brightness introduces significant distortion. Also,
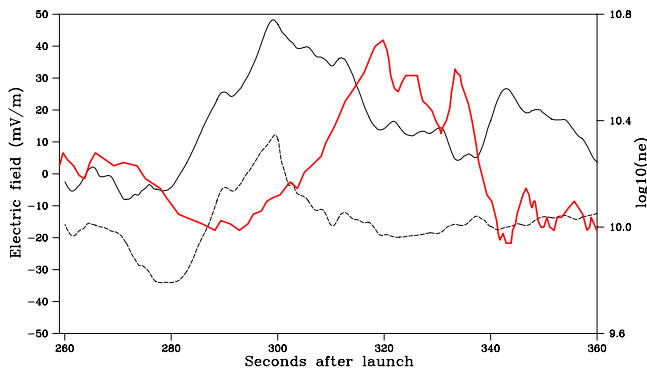
Figure 7. In situ electric field and density measurements made by the NASA JOULE rocket R36206 during downleg. Shown in geomagnetic coordinates are zonal electric field (regular line, west is positive), meridional electric field (dashed line, north is positive), and plasma density (gray line). The descent altitude range is approximately 200–150 km.

the bright spot located between the trajectories and near the center of the images is the trimethyl aluminium (TMA) release from another rocket for measuring the neutral wind.

[24] Through the times of the data set in Figure 6, we infer the following sequence of events on the equatorward side of the auroral arc (ordering follows the ordering of the images): (1) two NASA JOULE rockets (R21131 on the west side and R36206 on the east side) departed from Poker Flat with 3 min separation and first traveled approximately 100 km north-northwestward and northward through a region of southward electric fields with magnitudes between 40 and 80 mV/m; this region was coincident with strong radar backscatter, but there was no optical aurora; (2) R36206 exited this region and entered an approximately 30 km long path with westward electric fields in the range of 10–20 mV/m; radar backscatter here was absent, and there was no optical aurora yet; (3) while an auroral arc began to appear ahead in the northwest direction, this rocket entered another region in the vicinity of the arc and recorded enhanced electric fields in the range of 20–40 mV/m and pointing in the northwest direction; (4) radar backscatter immediately intensified behind this rocket on the equatorward side of the arc and mostly on the west side of this rocket's trajectory; only a glimpse of this backscatter intensification occurred at the exact rocket position; (5) meanwhile, R21131 continued to record a steadily large southward electric fields around 80 mV/m; (6) the electric field seen by R36206 turned southward. The electric field seen by R21131 decreased in magnitude while the direction remained the same. It appears that R21131 just reached the auroral arc's vicinity, but it is not clear if the electric field decrease can be associated with the auroral arc. Moreover, the information we infer here is mostly from the approach of the rockets to the arc. There is significant ambiguity regarding the precise location of the auroral arc on geographic coordinates and therefore it is not clear if the leading rocket passed through an arc or through the vicinity of auroral patches that are part of a larger-scale arc.

[25] One may argue that the relative positions of the arc and radar backscatter is ambiguous because the arc is near

the horizon and its location is ambiguous, but additional evidence suggests that the radar echoes occurred near the equatorward side of the arc. Figure 7 shows the in situ plasma density and electric field measurements made by the R36206 rocket as a function of seconds after its launch. We know from the animated sequence of radar images that, near 300 s (1214 UT), intense radar echoes occurred just behind or south side of the rocket position. These are the isolated echoes toward the north seen in the image set on the right-hand side of Figure 6. If the plasma density enhancement seen in Figure 7 between 300 and 340 s is a proxy for the auroral arc, the radar echoes occurred near the equatorward edge of the auroral arc.

[26] We understand from this set of events that a smooth, large-scale convection was interrupted by electric field structures associated with an auroral arc to the north. We further observe that there exist regions where the radar aurora is seen with no visible aurora nearby. Such cases occurred during mostly undisturbed, smooth, but enhanced convections, such as during the passage of the rockets through the first, mostly uniform flow region.

3. Summary

[27] We have presented high-resolution 30 MHz radar backscatter imaging observations of auroral plasma irregularities localized in the vicinity of auroral arcs and inferred the plasma convection from the Doppler data. We have also presented a case study in which radar and optical observations were presented together with in situ rocket electric field measurements. A summary of our findings is as follows:

[28] 1. The radar backscatter intensifications occurred almost simultaneously with discrete optical auroral intensifications measured by all sky cameras, auroral electrojet intensifications measured by magnetometers on the ground, and ultraviolet emission intensifications as measured by the ultraviolet imager on board the NASA's Polar spacecraft.

[29] 2. The poleward edges of the latitudinally aligned arcs were mostly accompanied by narrow radar backscattering structures aligned parallel to the arcs. The backscattering regions on the equatorward sides of these arcs were more spread. These observations are in accordance with the "diffuse" and "discrete radar aurora" description by the earlier literature [e.g., *Greenwald et al.*, 1973].

[30] 3. When there was discrete optical aurora, there was often radar aurora. However, there were cases of radar aurora without optical aurora, implying that the optical aurora is not a prerequisite for the radar aurora to occur.

[31] 4. The radar aurora was often observed at the discrete arc boundary and suppressed inside the arc. Radar aurora could sometimes be seen inside an arc at the very peak of optical intensification.

[32] 5. For stable arcs with well-defined poleward and equatorward boundaries, the radar echoes at these boundaries had opposite Doppler shifts, implying a convection reversal from one boundary to another. As inferred from the Doppler velocities, the electric fields at the boundaries pointed more toward the arc boundary, as opposed to away from it.

[33] The radar aurora appears to be more associated with discrete optical aurora. In fact, in Figure 3, range-
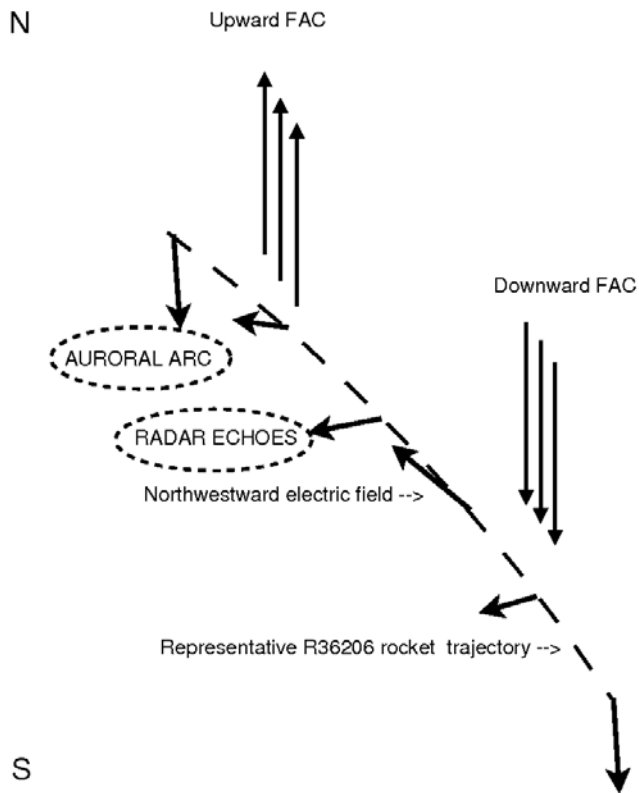
Figure 8. A cartoon of electric field and current structure near an auroral arc that is consistent with the optical aurora and NASA R36206 rocket electric field observations shown in Figure 6. The six vector electric fields are representative of the rocket measurements.

time-intensity plots of bursty, discrete optical and radar aurora show sharp correspondence, while after 1015 UT the auroral emissions appears to became diffuse and there is no radar backscatter. This may be attributed to the absence of strong diffuse auroral electric fields exceeding the two-stream instability threshold or the absence of strong density gradients in diffuse aurora.

[34] Radar aurora in the absence of optical aurora means that the ionospheric convection electric field exceeds a certain threshold for the two-stream instability, which is not a surprising occurrence in the auroral region. The suppression of the radar aurora inside the arcs meanwhile is an expected consequence of electron precipitation, which closely coincides with the optical aurora and electron density enhancements [*Pallamraju et al.*, 2001]. The enhancement of the ionization changes the ionospheric conductivity and reduces the electric field magnitude to a value below the threshold for the excitation of the two-stream instability. For example, the reduction of the electric field between 315 and 340 s in Figure 7 is probably because of electron density enhancement, which was perhaps due to auroral precipitation. As reported by *Bahcivan et al.* [2005], in the rocket frame, a concentration of radar backscatter occurred near 300 s, and the backscatter ceased in the following seconds after the electric field were lowered below the instability threshold. Furthermore, this suppression of radar backscatter can also be attributed to inhibition

of irregularity formation due to enhanced recombinative damping in increased plasma density.

[35] The reversal of the convection across an arc implies that in the vicinity of an arc, the electric field structure is determined by field-aligned currents. If auroral precipitation generated density structures polarized only by existing background convection, the electric fields at the opposing arc boundaries would be pointed in the same direction. Because the electric fields point more toward the arcs, we expect that these signify upward field-aligned currents. Moreover, based on what we infer from the sequence of events in the data set in Figure 6, in their approaches to the auroral arc, the rockets observed a region of divergent electric fields, as suggested by the almost complete reversal of the electric field as measured by the rocket R36206. This was probably the downward current region. A cartoon illustrating this picture is shown in Figure 8. It is possible that the northwestward electric field on the equatorward side of the arc was connecting these two field-aligned currents by driving a Pedersen current in the middle.

[36] There are a number of observations/predictions that sit on the same footing of field-aligned currents and convergent/divergent electric fields. Using EISCAT tristatic measurements of the electric field in the vicinity of auroral filaments and thin arcs, *Lanchester et al.* [1996] found strong divergent electric fields. Two- and three-dimensional simulations of auroral filaments [*Zhu et al.*, 2001; *Lanchester et al.*, 2001; *Otto and Zhu*, 2003] predict strong ionospheric electric fields and sheared plasma flow in the immediate vicinity of structured small-scale auroral arcs and associated upward field aligned currents. Meanwhile, a northward electric field on the equatorward side of a stable, east-west aligned arc was reported by *Aikio et al.* [2002] based on joint incoherent scatter radar and optical measurements and by *Janhunen et al.* [2000] based on joint measurements by the FAST satellite and the MIRACLE ground-based network of all-sky cameras, coherent radars, and magnetometers.

[37] The inferred electric field structure at the arc boundary has implications for the gradient drift mechanism. According to the growth rate expression for two-stream waves [*Fejer et al.*, 1975], if the electron density gradient scale length is sufficiently small and the gradient is parallel to the electric field large-scale (100–1000 m) gradient drift mechanism can be excited. Given that an arc's brightness is a proxy for the electron density, the electric fields we infer are antiparallel to the density gradients of auroral arcs, and therefore the gradient drift mechanism is stabilizing. *St.-Maurice et al.* [1994] presents a detailed description of how the density gradients affect short and long wavelength two-stream waves in the vicinity of discrete auroral arcs. For large scale waves, we actually expect an increase in the electric field threshold for the two-stream instability. However, we expect that for meter scale waves the increase is negligible.

[38] In summary, we predict that the 30 MHz E region radar aurora in the vicinity of a stable auroral arc is caused by the arc's polarization electric fields. If above threshold, the fields can excite the two stream instability and generate electron density irregularities at meter scales, which is the cause of radar aurora.

References

Aikio, A. T., T. Lakkala, A. Kozlovsky, and P. J. S. Williams (2002), Electric fields and currents of stable drifting auroral arcs in the evening sector, *J. Geophys. Res.*, *107*(A12), 1424, doi:10.1029/2001JA009172.

Bahcivan, H. (2005), Auroral electrojet irregularities, Ph.D. thesis, Cornell Univ., Ithaca, N. Y.

Bahcivan, H., D. L. Hysell, M. F. Larsen, and R. F. Pfaff (2005), The 30 MHz imaging radar observations of auroral irregularities during the JOULE campaign, *J. Geophys. Res.*, *110*, A05307, doi:10.1029/2004JA010975.

Balsley, B. B., W. L. Ecklund, and R. A. Greenwald (1973), VHF Doppler spectra of radar echoes associate with a visual auroral form: Observation and implications, *J. Geophys. Res.*, *78*, 1681.

Fejer, B. G., D. T. Farley, B. B. Balsley, and R. F. Woodman (1975), Vertical structure of the VHF backscattering region in the equatorial electrojet and the gradient drift instability, *J. Geophys. Res.*, *80*, 1313.

Greenwald, R. A. (1995), Superdarn: A global view of high-latitude convection, *Space. Sci.*, *71*, 763.

Greenwald, R. A., W. L. Ecklund, and B. B. Balsley (1973), Auroral current, irregularities, and luminosity, *J. Geophys. Res.*, *78*, 8192.

Hysell, D. L. (1996), Radar imaging of equatorial *F* region irregularities with maximum entropy interferometry, *Radio Sci.*, *31*, 1567.

Hysell, D. L., and J. L. Chau (2006), Optimal aperture synthesis radar imaging, *Radio Sci.*, *41*, RS2003, doi:10.1029/2005RS003383.

Janhunen, P., A. Olsson, and K. Kauristie (2000), Characteristics of a stable arc based on FAST and MIRACLE observations, *Ann. Geophys.*, *18*, 152.

Lanchester, B. S., K. Kailá, and I. W. McCrea (1996), Relationship between large horizontal electric fields and auroral arc elements, *J. Geophys. Res.*, *101*, 5075.

Lanchester, B. S., M. H. Rees, and D. Lummerzheim (2001), Ohmic heating as evidence for strong field-aligned currents in filamentary aurora, *J. Geophys. Res.*, *106*, 1785.

Milan, S. E., M. Lester, N. Sato, and H. Takizawa (2001), On the altitude dependence of the spectral characteristics of decametre-wavelength E region backscatter and the relationship with optical auroral forms, *Ann. Geophys.*, *19*, 205.

Milan, S. E., N. Sato, Y. Muraya, Y. Shinkai, H. Doi, H. U. Frey, and T. Saemundsson (2003), E-region echo caharacteristics governed by auroral arc electrodynamics, *Ann. Geophys.*, *21*, 1567.

Otto, A., and H. Zhu (2003), Fluid plasma simulation of coupled systems: Ionosphere and magnetosphere, *Space Plasma Simul.*, *615*, 193.

Pallamraju, D., J. Baumgardner, S. Chakrabarti, and T. R. Pedersen (2001), Simultaneous ground based observations of an auroral arc in daytime/twilight time oi 630 nm emission and by incoherent scatter radar, *J. Geophys. Res.*, *106*, 5543–5549.

Prikryl, P., and L. L. Cogger (1992), Statistical analysis of the spatial relationship between the radio aurora and optical aurora: Further evidence for refraction, *Radio Sci.*, *27*, 4, 469–479.

Providakes, J. F., D. T. Farley, W. E. Swartz, and D. Riggin (1985), Plasma irregularities associated with a morning discrete auroral arc: Radar interferometer observations and theory, *J. Geophys. Res.*, *90*, 7513.

St.-Maurice, J. P., P. Prikryl, D. Danskin, A. M. Hamza, G. J. Sofko, J. A. Koehler, A. Kustov, and J. Chen (1994), On the origin of narrow non-ion-acoustic coherent radar spectra in the high latitude *E* region, *J. Geophys. Res.*, *99*, 6447.

Tsunoda, R. T., R. I. Presnell, Y. Kamide, and S. I. Akasofu (1976), Relationship of radar aurora, visual aurora, and auroral electrojets in the evening sector, *J. Geophys. Res.*, *81*, 6005.

Watermann, J. (1990), Refraction of 50-MHz radar waves in a realistic ionospheric model, *Radio Sci.*, *25*, 805.

Zhu, H., A. Otto, and D. Lummerzheim (2001), Ionosphere-magnetosphere simulation of small-scale structure and dynamics, *J. Geophys. Res.*, *106*, 1795.

————————

H. Bahcivan, Center for Geospace Studies, SRI International, 333 Ravenswood Avenue, G287, Menlo Park, CA 94025, USA. (hasan.bahcivan@sri.com)

D. L. Hysell, Department of Earth and Atmospheric Sciences, Cornell University, 2108 Snee Hall, Ithaca, NY 14853, USA. (daveh@geology.cornell.edu)

D. Lummerzheim, Geophysical Institute, University of Alaska, 903 Koyukuk Drive, Fairbanks, AK 99775-7320, USA.

M. F. Larsen, Department of Physics and Astronomy, Clemson University, Clemson, SC 29634, USA.

R. F. Pfaff, NASA Goddard Space Flight Center, Code 696, Greenbelt, MD 20771, USA.